Ocean Engineering 259 (2022) 111899

Contents lists available at ScienceDirect

Ocean Engineering

journal homepage: www.elsevier.com/locate/oceaneng

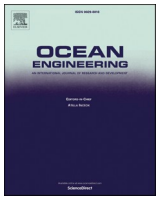

Offshore inspection mission modelling for an ASV/ROV system

Chenyu Zhao [a,*], Philipp R. Thies [a], Lars Johanning [a,b]

[a] Renewable Energy Group, College of Engineering, Mathematics and Physical Sciences, University of Exeter, UK
[b] Naval Architecture, Harbin Engineering University, Nantong Main Street 145, Nangang District, Harbin, China

ARTICLE INFO

Keywords:
Offshore
Inspection
ROV
ASV
LARS
Numerical model

ABSTRACT

To reduce the human exposure risk during the offshore structure inspection, the Remotely Operated underwater Vehicle (ROV) is a widely used solution. This paper couples an inspection class ROV with an autonomous surface vehicle (ASV) via a launch and recovery system (LARS) in a nonlinear numerical model. Operational inspection missions with both static and moving targets are modelled for this ASV/ROV system. The paper reports the following distinctive mission profiles: i) pipeline inspection, ii) floating offshore wind turbine (FOWT) mooring line inspection and iii) circumferential weld surface scan at the FOWT spar. The results provide important parameters to design and implement autonomous inspection missions. During the scan/check stage, the distance between the ROV and the target will be varying, due to the relative motion between the ASV and ROV. Important model results are that missions with following ASV will allow to reduce the ROV umbilical tension for a given mission profile. Results also determined that the net buoyancy of the ROV will lead to a position offset. In the surface scan cases, it is found that the drag force caused by the tidal current can contribute to ROV rotation and should be considered in detail ahead of any mission.

1. Introduction

The current stage of traditional and renewable offshore energy industry, is now contributing to an attractive energy mix around the world, thus leading to increasing investments/number in the offshore structures as well as the demand for inspection and maintenance (Fazeres-Ferradosa et al., 2019; Khojasteh et al., 2018; Yuh et al., 2011). As with any offshore operation, there is an incident risk. ROVs are widely used to reduce the incidents during the offshore structure's inspections, (Capocci et al., 2017; Choi et al., 2017; Yuh, 1990). ROVs can be categorised into inspection-class and intervention-class vehicles, the former is more suitable for the inspection tasks owing to its lower cost, smaller mass and more accessible design (Trslić et al., 2018). The rated depth of inspection ROV is usually less than 300 m, and the mass is below 200 kg. This small mass design allows the inspection ROV to be manually recovered in some extreme conditions.

In natural sea environments, ROV inspection tasks are always carefully designed based on their inspection objectives, including the static and moving types. As most conventional targets are static, they can be accurately located. The ROV control strategy is relatively straightforward for static targets but becomes more complex for moving targets. The ROV control strategy for static targets can allow ROV to operate with a pre-designed path to approach the targets. Subsea pipeline and its related structures such as riser, spool piece, landfall, etc. (see Fig. 1) are the most common static inspection objectives. Considering the pipeline's failure will bring a very significant environmental and production loss and their repairs/replacements have a very high cost and risk, the pipeline inspections had led to substantial worldwide industrial and safety concerns (Braathen and Sandford, 1986; Salgado-Jimenez et al., 2010). According to the data reported by the U.S. Department of Transportation Pipeline and Hazardous Materials Safety Administration (PHMSA), just in 2020, 17 people lost their lives, and the 27 people injured in pipeline accidents and the related economic loss exceeded 200 M dollars(Administration, 2021). In the U.K., the safe management of both onshore and offshore pipelines is controlled by the Pipelines Safety Regulations (PSR) 1996, which requests regular and safe inspections "…the operator shall ensure that a pipeline is maintained in an efficient state, in efficient working order and in good repair…the pipeline operator needs to consider both how and when the pipeline should be surveyed and examined to validate and maintain it is, in a safe condition…" (Books, 1996). Subsea pipeline inspections faces several significant challenges. Ho et al. (2020) gave a very comprehensive review of the subsea pipeline inspection and its multiple issues and obstacles, such as large hydrostatic pressure, low temperature and chemical attack.

* Corresponding author.
E-mail addresses: c.zhao@exeter.ac.uk (C. Zhao), P.R.Thies@exeter.ac.uk (P.R. Thies), L.Johanning@exeter.ac.uk (L. Johanning).

https://doi.org/10.1016/j.oceaneng.2022.111899
Received 28 May 2021; Received in revised form 29 March 2022; Accepted 2 July 2022

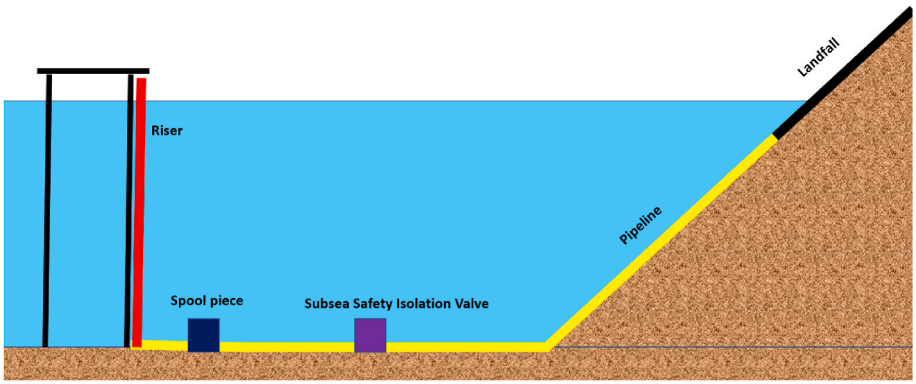

Fig. 1. Illustration of typical pipeline system (not to scale).

A range of sensor technologies and their strong/weak points such as magnetic flux leakage (Mandache and Clapham, 2003; Shi et al., 2015), ultrasound pulse-echo (Marció et al., 2019; Skjelvareid et al., 2013), Ultrasonic-guided wave testing (Marques and Demma, 2008; Rose, 2004), Sonar (Hansen et al., 2010), Fibre optics (Tanimola and Hill, 2009; Wang and Wang, 2010), were also reported. The ROV is usually equipped with these sensors for leakage pipeline inspection.

The moving inspection objectives are usually known as floating structures/vessels, like the ship, floating offshore wind turbines (FOWT), floating platforms. In a typical scenario for moving objectives inspection, the vehicle may be programmed to check the mooring system and the structure surface layer. As the moving targets will be activated by the environmental load (wave, tidal current, and wind), it is favourable to seek position and distance measurements relative to the floating structure, rather than the fixed distance and the pre-designed path. As a result, the control strategy of ROVs is more challenging to design, and the equipped sensors will be more complex and expensive (Christ and Wernli Sr, 2011; Gordon et al., 2014). The ROV for the traditional floating structures inspection has been widely applied and successfully demonstrated. For example, an ROV is designed to inspect and monitor the surface of large oil ship hulls and floating production storage and offloading platforms. An algorithm navigates the ROV based on an extended-Kalman-filter (EKF) sensor-fusion formulation (Menegaldo et al., 2009). Other similar successful examples of ship hull inspection can be found in (Menegaldo et al., 2008; Negahdaripour and Firoozfam, 2006). The demand for FOWT inspection is also increasing rapidly. Because FOWTs usually operate in a harsh environment (strong wind and waves), the failure rate of the FWOT is relatively higher than the onshore wind turbine (Carroll et al., 2016). The potential incidents rate is also increased during the FOWT inspection. The G + Global Offshore Wind Health and Safety Organisation monitor and reports incident data. Their 2019 incident data report (Organisation, 2020) listed 865 health and safety incidents, of which 245 occurred on vessels. A third of 252 high potential incidents, defined as incidents having the potential to cause fatalities, occurred on Crew Transfer Vessels. Thus, ROVs present the opportunity to gradually reduce this risk, particularly for far offshore farms with over 100 km distance-to-shore. Some recent studies like (Martinez-Luengo and Shafiee, 2019; Sheppard et al., 2010; Sivčev et al., 2017) have demonstrated the high potential and the feasibility of the ROV for the FOWT inspection. These studies mainly explore the feasibility of overall maintenance strategies, but do not explore the detailed technical aspects of autonomous inspection missions. Conte, De Capua et al. (2016) gave the design method of Navigation, Guidance and Control system of the ASV. Several studies were also conducted to module ASV/ROV system and applied them in a range of fields (Conte et al., 2020; Conte et al., 2016; Jung et al., 2018; Sarda and Dhanak, 2016; Wang et al., 2008).

This study promotes a fully coupled numerical model with independent module design and high compatibility. In this model, the ROV

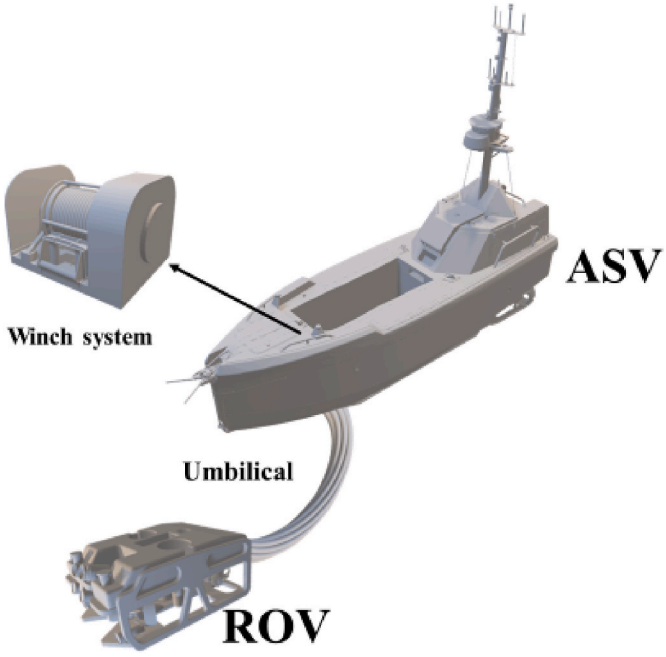

Fig. 2. The ASV/ROV autonomous inspection system.

can be launched and recovered from an ASV by a LARS with the given control strategies. This study models cases with both static and moving inspection targets for the presented ASV/ROV system:

- Pipeline inspection (static targets)
- FOWT morning line segment check (moving targets)
- FOWT spar surface scan (moving targets)

This paper is organised as follows: Section 2 introduces the ASV/ROV inspection system; Section 3 presents the ASV/ROV system's performance with the static and moving targets. Section 4 discusses the main findings considering potential industrial applications and further R&D requirements. Section 5 concludes with the main results and outcomes.

Table 1
The properties of the CW7 (L3HARRIS, 2020).

Property	Value (unit)
Length	7.2 m
Beam	2.3 m
Draft	0.9 m
Weight (without payload)	4280 kg

Table 2
Properties of the modelled ROV (SEAEYE, 2020).

Property	Value (unit)
Length	1 m
Width	0.6 m
Height	0.5 m
Weight in the air (with the max payload)	74 kg
Weight in the water	5 kg
Max thrust	Forward = 50 *kgf* *Lateral* = 28 *kgf* *Vertical* = 13 *kgf*

Table 3
Properties of the umbilical and winch.

Property	Value (unit)
Diameter	0.17 *m*
Weight in air	350 *kg*/*km*
Weight in water	150 *kg*/*km*
Minimum dynamic bending diameter	350 *mm*
Breaking strength	18 *kN*
Max allow tension	3 *kN*
Winch drum diameter	0.5 m
Winch drum mass	50 kg

2. System design and modelling

2.1. ASV/ROV design

The presented autonomous inspection system includes an ASV (named as CW7), an ROV and a LARS, and each part can be independently or interactively controlled (Fig. 2). The physical properties of the system are listed in Tables 1–3.

2.2. ASV/ROV modelling

The ASV/ROV system is modelled via a frequency-time domain approach. Firstly, the hydrodynamic coefficients of ASV, ROV and the FOWT spar are calculated in the frequency model with the AQWA solver (ANSYS, 2013). The coupled effects on the hydrodynamic coefficients are also considered. Then, frequency-domain results are transferred into the time-domain where the nonlinear factors like control forces and torque can be managed (the solver is the Orcaflex (Manual, 2012)). The overview of the numerical model is presented in Fig. 3.

The ASV/ROV system's hydrodynamic model has been established and validated in our previous research(Zhao et al., 2020, 2021). This section mainly focuses on the new ASV/ROV system's control strategies for the three cases presented in Section 1. The dynamic functions of ASV, ROV and the umbilical are also provided in the Appendix for reference.

We adopt the following terminology: A 'following ASV' denotes that the ASV follows the ROV during the operation, whereas a 'static ASV' denotes that the ASV holds its position.

The control force matrix of the following ASV in current paper is:

$$[C]=\begin{bmatrix} (x_{ROV}-x_{ASV}-x_{dis\ tan\ ce})*k_{lx}*log_2(z_{ASV}-z_{ROV}) & 0 & 0&0&0&0\\ 0 & (y_{ROV}-y_{ASV}-y_{dis\ tan\ ce})*k_{lx}*log_2(z_{ASV}-z_{ROV}) & 0&0&0&0\\ 0 & 0 & 0&0&0&0\\ 0 & 0 & 0&0&0&0\\ 0 & 0 & 0&0&0&0\\ 0 & 0 & 0&0&0&0 \end{bmatrix} \quad (1)$$

where x_{ROV}, y_{ROV} are the position of ROV, $x_{dis\ tan\ ce}, y_{dis\ tan\ ce}$ are the distance between ASV and ROV.

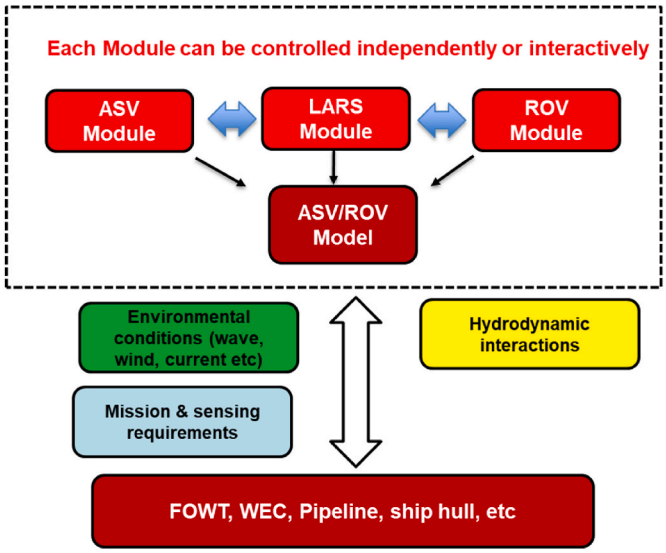

Fig. 3. The overview of the ASV/ROV numerical model.

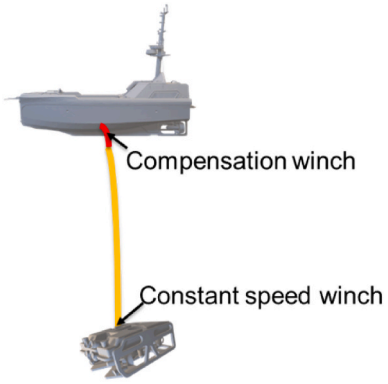

Fig. 4. The LARS design of the ASV/ROV system.

When the ASV hold its position, the above the control force matrix will be replaced by:

$$[C]=\begin{bmatrix} C_1(x_{ASV}-x_0) & 0 & 0&0&0&0\\ 0 & C_2(y_{ASV}-y_0) & 0&0&0&0\\ 0 & 0 & 0&0&0&0\\ 0 & 0 & 0&0&0&0\\ 0 & 0 & 0&0&0&0\\ 0 & 0 & 0&0&0&0 \end{bmatrix} \quad (2)$$

For the ROV, the control method on the x, y direction offers a gentle way for the propeller force to increase as a function of its depth to the ASV:

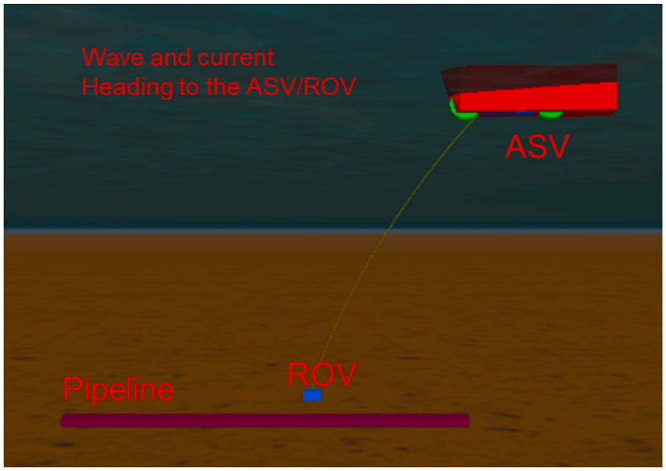

Fig. 5. ROV deployment of the pipeline inspection case, the initial ROV position in this case is (−8,0, −4).

$$F_{lx} = \left(x_{target} - x_{ROV}\right) * k_{lx} * log_2\left(z_{ASV} - z_{ROV}\right) \tag{3}$$

$$F_{ly} = \left(y_{target} - y_{ROV}\right) * k_{ly} * log_2\left(z_{ASV} - z_{ROV}\right) \tag{4}$$

$$F_{lz} = \left(z_{target} - z_{ROV}\right) * k_{lz} * log_2\left(z_{ASV} - z_{ROV}\right) \tag{5}$$

When F_{lx}, F_{ly} and F_{lz} are larger than the maximum ROV thrust, the maximum thrusts will replace them.where $x_{target}, y_{target}, z_{target}$ are the target coordinates in each direction; k_{lx}, k_{ly}, k_{lz} are the launch control coefficients in each direction.

The LARS modelled here includes a constant speed winch and a motion compensation winch (Huster et al., 2009), significantly reducing the umbilical tension and stabilising the whole system(Fig. 4).

The whole winch pay-out velocity is defined as:

$$V_{out} = V_{fix} + V_{com} \tag{6}$$

where V_{fix} is the winch speed which is either constant or linearly variable with time and V_{com} is the compensation winch speed.

The compensation winch drive force is:

$$F_{drive} = F_{target} + F_{resistance} \tag{7}$$

where F_{target} is the target tension on the umbilical.

The resistance of the winch could be presented as:

$$F_{resistance} = d_{db} + c_{out} v_{out} + d_{out} v_{out}^2 \tag{8}$$

where d_{db} is the winch drive dead-band, c_{out} are the winch drive damping terms for pay-out. d_{out} are the winch drive drag terms for pay-out.

According to equations (6) and (7) and $J_{winch} = M_{winch} R_{winch}^2$

$$v_{out}(s \quad t) = \frac{\left(F_{target} - T_{tension}\right)}{M_{winch} R_{winch}} t + v_{out}(s_0 \quad 0) \tag{9}$$

When the compensation system operates within a safe range, the target tension is constant:

$$F_{target} = F_{reuqired} \tag{10}$$

When the relative motion between the ASV and ROV exceeds the capacity of the compensation system, i.e. if the motion amplitude of the cylinder/drum (s_c) > max threshold limit of the safe range ($s_{\max}$), the target tension is set to:

$$F_{target} = F_{reuqired} + c_t\left(s_{\max} - s_c\right) \tag{11}$$

If $s_c < s_{\min}$, $s_{\min}$ is the min threshold limit of the safe range.

$$F_{target} = F_{reuqired} + c_t\left(s_{\min} - s_c\right) \tag{12}$$

where the c_t is the control coefficient in the tension control.

2.3. Target modelling

As described in Section 1, three cases (pipeline inspection, FOWT mooring inspection and a spar surface scan) are considered here to simulate the real sea environment's inspection missions. The individual mission profiles are briefly outlined in the following.

For the Subsea pipeline inspection cases (Fig. 5), the ROV is firstly launched from a static ASV (with Eq. (2)) to the pipeline (launch stage), and the ROV tracks along the pipeline with a fixed height (inspection stage). During the inspection stage, the static ASV will transfer to a following ASV (with Eq. (1)).

For the mooring segment inspection, the selected FOWT is the NREL-5MW (Jonkman et al., 2009), which is publicly available (OrcaFlex, 2021), fully and widely used as a reference case. It is fully validated. The position of the mooring line segment is regarded as the target position of the ROV, which will be updated in each time step. The ROV thrust will be consequently adjusted by Eq. (2) to Eq. (4).

For the surface scan case, the ROV will always head to the scan surface. Owing to the fact that the surface is curved, additional torque (Eq. (13)) is required to control the ROV heading direction.

$$M_{ROV} = c_{ROVh}\left(\theta_{targeth} - \theta_{ROVh}\right) \tag{13}$$

where c_{ROVh} is the ROV control coefficient, $\theta_{targeth}$ is the ROV target heading angle and the θ_{ROVh} is the ROV current heading angle.

At the FOWT design stage, the location sensor of the spar and the vital part of the mooring system should be considered, allowing the ROV to calculate the inspection targets.

$$TargetX = [X_M + d\sin(\theta)] + R\cos(\theta) * \cos(\omega t) \tag{14}$$

$$TargetY = R * \cos(\varphi) * \sin(\omega t) + [Y_M + d\sin(\varphi)] \tag{15}$$

$$TargetZ = Z_M + d\cos(\theta)\cos(\varphi) \tag{16}$$

And the ROV local heading direction is

$$TargetHeading = \omega t \tag{17}$$

where (X_M, Y_M, Z_M) is the position of the spar mass centre, d is the distance between the surface and the mass centre along with the spar, R is the radius of the spar,θ is the pitch of the spar, φ is the roll of the spar, ω is the scan angle velocity related to the vertical axis of the spar.

2.4. Environmental and control parameters

The approaching waves are identical in all cases and defined by a JONSWAP spectrum with the significant wave height $H_s = 2$ m and peak wave period $T_P = 5$s (Fig. 7). The tidal current velocity is calculated by a power law, allowing the velocity to decrease from the water surface to the seabed continuously. Fig. 8 gives an example to show the current velocity distribution along with the 100 m water depth.

$$S_c = S_b + \left(S_f - S_b\right)\left[\frac{z - z_b}{z_f - z_b}\right]^{1/p} \tag{18}$$

where S_c is the current speed at a z location. S_f and S_b are the current speeds at the surface and the seabed, respectively; p is the power-law exponent (Here is 7); z_f is the z-coordinate of the still water level; z_b is the z-coordinate of the seabed.

The control parameters of the ASV/ROV system used in this paper are listed in Tables 4–6.

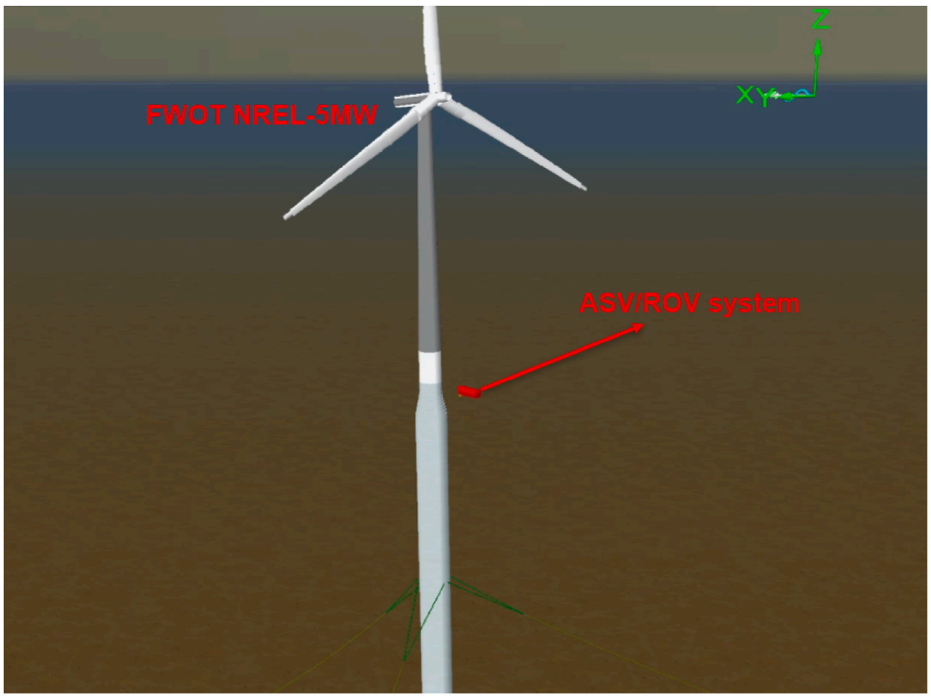

(a)

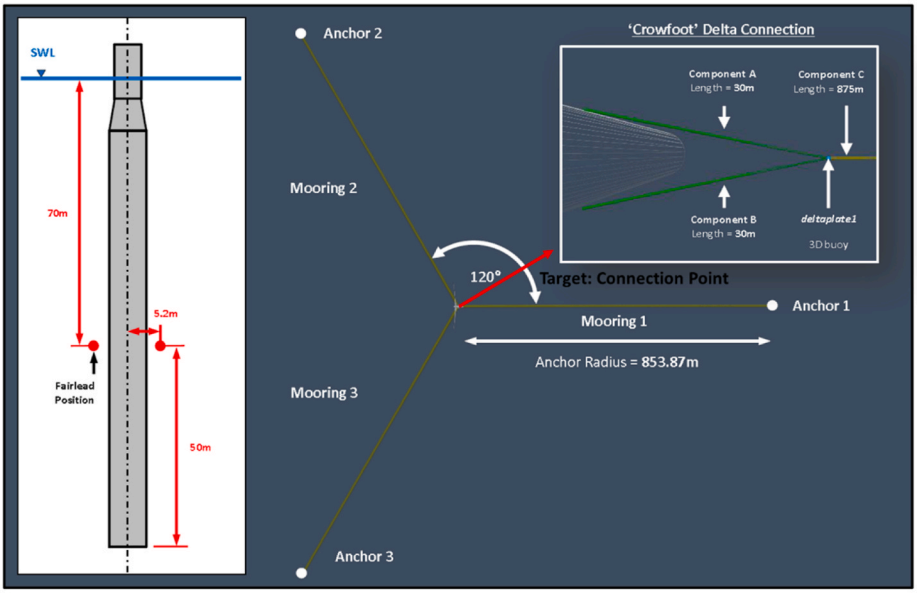

(b)

Fig. 6. The deployment of the FOWT mooring line inspection: (a) The overview of the FOWT and the ASV/ROV; (b) The target location(OrcaFlex, 2021).

3. Results

The result of the distance between the ROV and the target is vital for an inspection task. Large fluctuation of this distance poses a collision risk, which may not be acceptable. Another important factor is the umbilical tension. An umbilical with high tensile strength, usually has additional armour wiring and thus weight which will largely occupy the limited ASV payload. As a result, the performances of the ROV and the LARS with the given control strategy are presented in this section, aiming to support the ASV/ROV system design in reducing the required tensile rating and thus weight of the umbilical.

In the pipeline inspection case, the water depth is 30 m and the pipeline is located on the seabed. The flight height of the ROV is 1 m. Other details are presented in Table 7. As the initial y-position of ASV/ROV are identical to that of the pipeline, the results of the y-direction position are not presented here (Fig. 9 and Fig. 10). The ASV holds its position whilst the ROV approaches the scan start point ($t < 100s$) and then follows the ROV with a desired distance (0 m). For the LARS, V_{fix} is

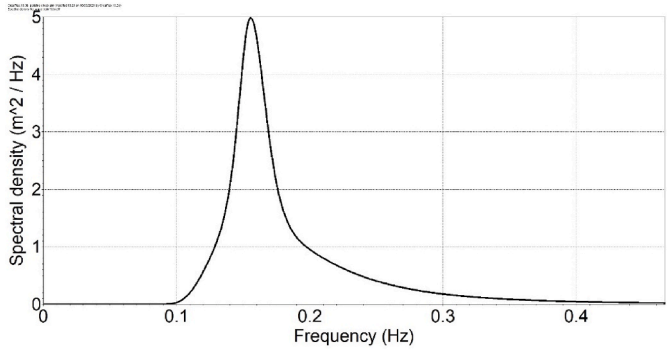

Fig. 7. The irregular wave defined by a JONSWAP spectrum: $H_s = 2$ m and $T_p = 5$s.

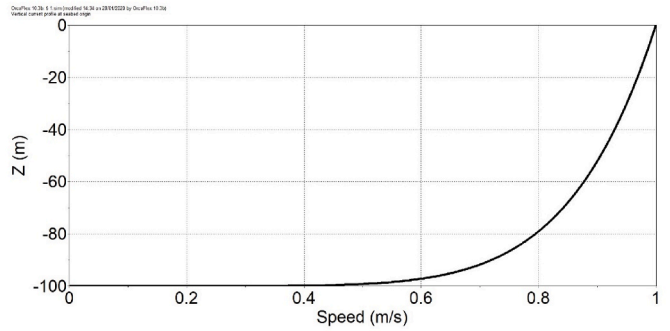

Fig. 8. Tidal current profile with 100 m water depth, exponent $p = 7$.

0.3 m/s during the ROV launching stage (t < 100s) and 0 m/s during the ROV inspection stage (t > 100s). The umbilical tension and V_{com} are presented in Fig. 11. These results show the umbilical tension does not exceed its minimum break load (MBL) 3 kN.

In the FWOT mooring line check case, the water depth is 320 m. A static ASV is selected with the ROV's initial position (1, 6, −4). The initial position of the ROV inspection target (Fig. 6) is (1, 24, −88). Fig. 12 presents the distance between the ROV and the moving targets. And the LARS performance is shown in the Fig. 13. It is observed that the ROV can reach/follow the targets under each direction with some distance fluctuations. Additionally, the maximum tension on the umbilical is smaller than the MBL.

In the FOWT surface scan case, the ROV control is identical to that in the mooring line check case while additional control torque is required to ensure the ROV always heads to the scan surface during scan stage (from 40s to 100s). The scan path is a 60-degree arc with a 1.5 m distance to the surface of the FOWT spar (Fig. 14). Fig. 15 presents the additional torque and its local heading angles. The distance between the ROV and the surface of the FOWT spar and the performance of the LARS are shown in the Fig. 16 and Fig. 17, respectively. These results show that the ROV can complete the rotation and can maintain its distance with a safe umbilical tension throughout.

Table 4
Control parameters of the ASV.

Static ASV	Following ASV
$C_1 = C_2 = 10kN/m$	$x_{dis\ tance} = 0m$ $y_{dis\ tance} = 0m$

Table 5
Control parameters of the ROV.

Control parameters	
k_{lx}	0.5 kN/m
k_{ly}	0.1 kN/m
k_{lz}	0.3 kN/m
C_z	0.1 kN
c_{ROVh}	0.1 $kN{\cdot}m$/deg
ω	1 deg/s

Table 6
Control parameters of the LARS.

Control parameters	
$F_{reuqired}$	1 kN
c_t	0.3 kN/m
$s_{\min}$	4.5 m
$s_{\max}$	5.5 m

Table 7
Operational parameters of the pipeline inspection case.

Properties	Unit (m)
ASV initial position	(-8,0,0)
Pipeline check Start	(-8,0,-29)
Pipeline check End	(-12,0,29)

4. Discussions

This paper modelled both static and moving objectives for inspection tasks with an ASV/ROV system via fully coupled numerical models. Results in Section 3 presented the overall performance of the ASV, ROV, and the LARS, demonstrating the potential, feasibility, and advantage of modelling offshore inspections with autonomous ASV/ROV systems.

In the pipeline check cases, the ASV can keep the fixed location very well for t < 100s; however, a relatively more significant distance between the ASV and ROV is observed during the ASV following stage (Fig. 9). It is believed that the following task brings more challenges for the ASV under the control strategy given in this study. This maximum

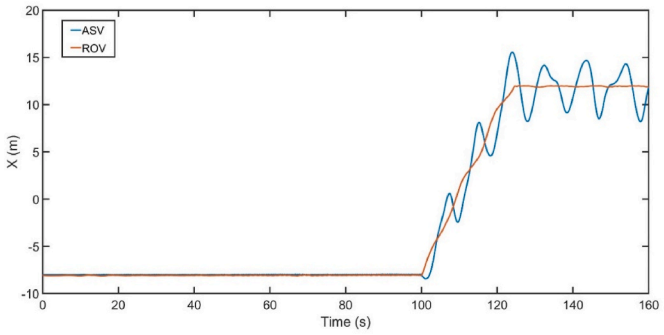

Fig. 9. Pipeline inspection case x-position of the ASV and the ROV.

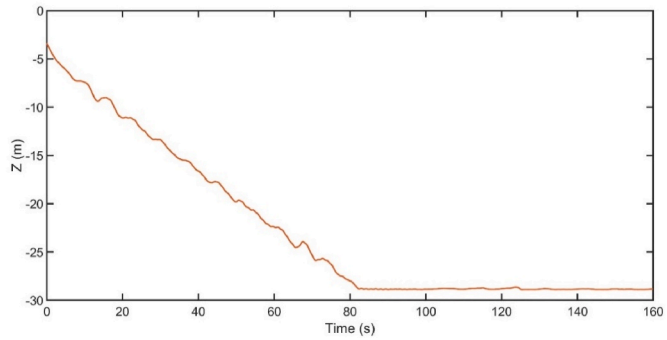

Fig. 10. Pipeline inspection case z-position of ROV.

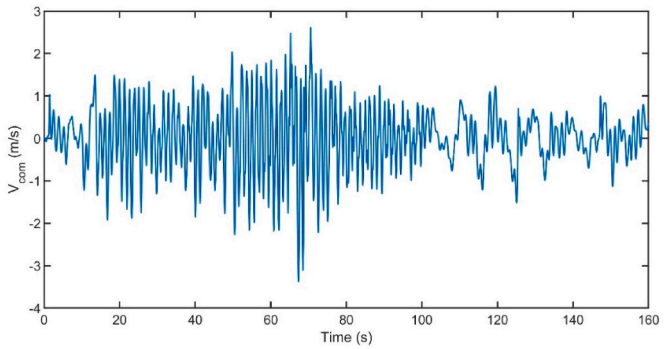

(a)

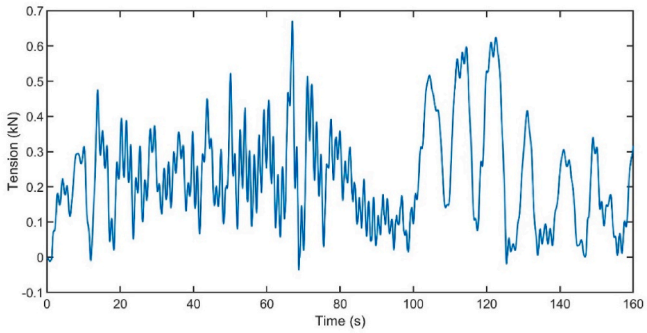

(b)

Fig. 11. Performance of the LARS in the Pipeline inspection case (a)V_{COM},(b) Umbilical tension, below the MBL 3 kN.

amplitude of the relative distance between ASV and ROV can reach 4.2 m, shown in Fig. 18. The following ASV, in this case, did not reduce the umbilical tension amplitude while it significantly stabilises the tension [Fig. 11 (b)]. As a result, the compensation winch speed requirement is decreased accordingly [Fig. 11 (a)]. Fig. 19 shows the ROV fly height during the inspection stage. It is found that the ROV operates at a slightly higher position compared to the desired fly height. This is because of the positive net buoyance of the ROV when the ROV is fully submerged. According to Eq. (5), the ROV needs a small distance (approximate 0.1 m in this study) to generate the control force to offset this net buoyance. This should be taken into account when determining the inspection distance. Additionally, fluctuations of the ROV fly height are observed, which is believed to be caused by the relative motion between the ASV and the ROV (up to 0.4 m in this study). In reality, both the ROV net buoyancy and the fly height fluctuations should be considered during the control system/strategy design.

In the FOWT mooring inspection case, the ROV and the target share the same initial position. Thus, the ROV has a better performance in tracking the moving target in the x-direction, compared to the y and z-directions (Fig. 12). In z-direction, the offset distance to the target, due to the net buoyancy is still approximate 0.1 m, which is the same as in the static target case. However, the amplitude fluctuation of the distance between ROV and target is smaller (comparing Figs. 19 and 20). An apparent tension reduction is observed for the umbilical tension after the ROV reached the target on the y-direction. The ratio between V_{fix} the ROV speed becomes larger when ROV only has the approaching speed in z-direction, emphasising the Lazy-Wave shape of the umbilical, resulting in a smaller tension. The study does not explore this speed ratio in detail at the current stage, but it is worthy of discussion in further research. It seems that a relatively longer umbilical or a faster pay-out rate will

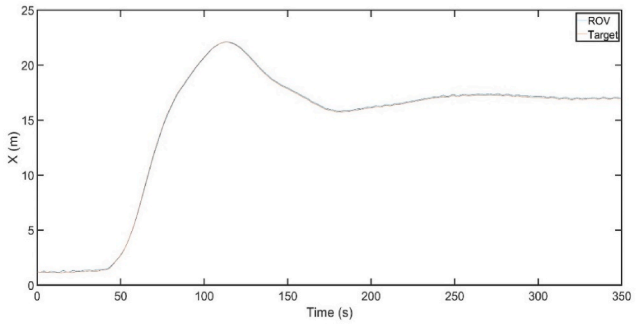

(a)

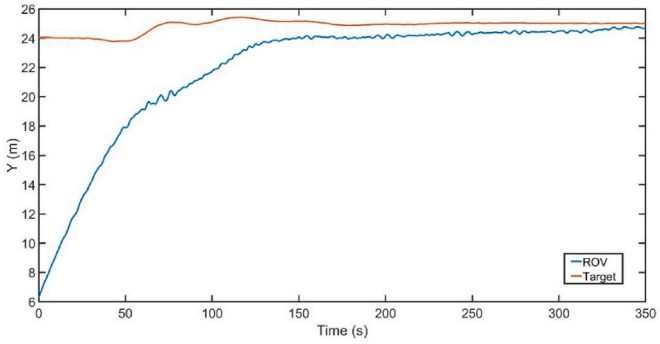

(b)

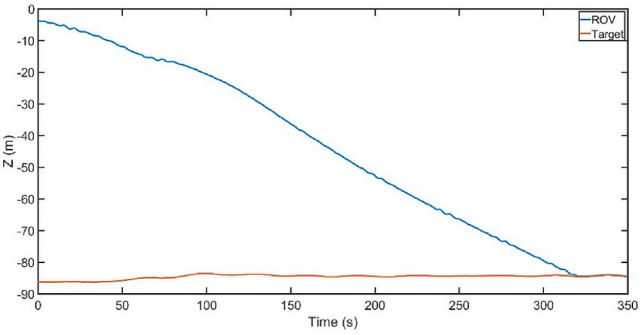

(c)

Fig. 12. Distance between ROV and ASV (a) X-direction, (b) Y-direction, (c) Z-direction.

reduce the tension. This aspect will have to be balanced with the allowable minimum bending radius of the umbilical. A longer umbilical has a greater risk of entanglement between the umbilical and the inspection objective (especially with mooring lines). In this case, a close distance (less than 1 m) is found between the FOWT spar and the umbilical.

In the FOWT surface scan case, the ROV relies on an additional torque to head to the spar surface. This torque only exists at the beginning and last 5 s of the scan stage. It can be observed that the heading torque is almost zero in most of the scan stage (Fig. 15). In this case, the tidal current direction is parallel to the ROV (opposite). When the ROV begins to alter its heading direction, the hydrodynamic force caused by the tidal current will help the ROV rotate. The ROV control torque is chosen to adjust the ROV rotation speed in line with the desired scan speed. For the given ROV, the hydrodynamic force can keep the

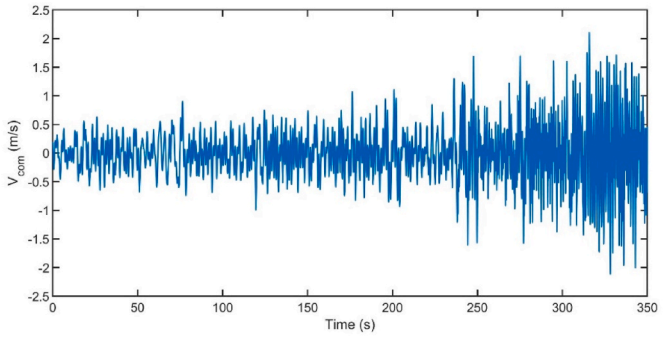

(a)

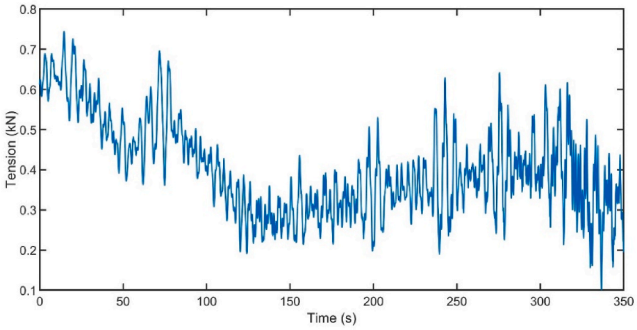

(b)

Fig. 13. Performance of the LARS in the mooring inspection case (a)V_{COM} (b) umbilical tension.

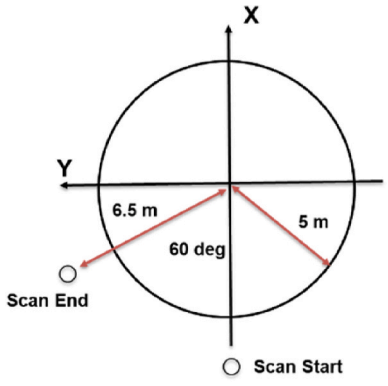

Fig. 14. Deployment of the scan cases under the Spar local coordinate.

ROV rotating with the desired speed during the scan stage. This consideration can reduce the energy consumption of ROV during the scan stage, but the ROV has to overcome the tidal current to reach the scan start point (here, the tidal current direction is assumed to be constant during the task). The scan path and speed should thus be carefully considered based on the expected sea conditions and the ROV capability. The distance variations between the ROV and the spar surface during the scan stage are similar to that in the FOWT mooring line check case (from 0.1 m to 0.2 m). Compared to that in the pipeline cases, the fluctuations are smaller in FOWT cases (Figs. 18 and 21). For cases where the ROV is supported by the following ASV, it will be more challenging to keep a fixed distance to the target. Furthermore, the ROV has already reached the target depth before the scan start point (at 35s), but the constant winch keeps paying out the umbilical, which causes a very small tension

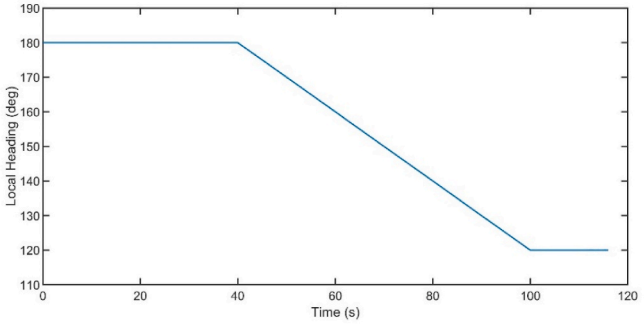

(a)

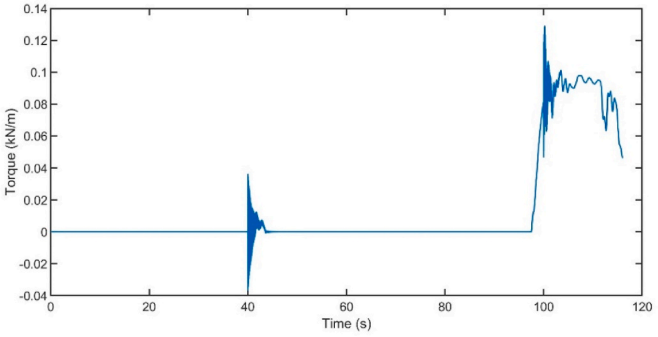

(b)

Fig. 15. ROV Heading and the additional torque (a) ROV heading angle. (b) Control torque.

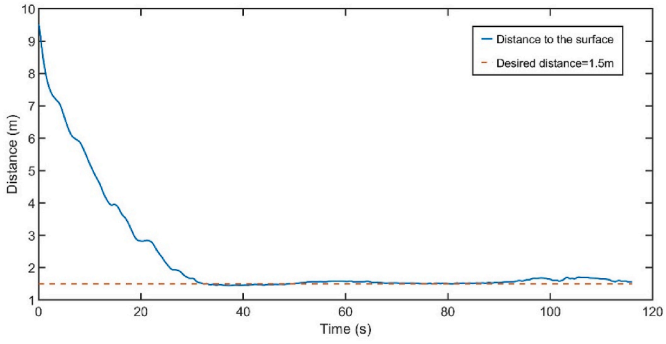

Fig. 16. The Distance between the ROV and the spar surface.

(from 35s to 80 s, seen in Fig. 17). Shown in Fig. 22, the spar has a significant lateral motion on the x-direction 50s. Because the ROV will keep a fixed distance from the spar, this motion accordingly increases the umbilical tension.

The results of this paper rely on the ability to track the accurate locations of the ROV and the inspection targets. In practice, the ROV may employ multi-sensors in parallel to detect/track a range of target profiles. The echo sounder is a realistic positioning technique that can be used to detect the distance between the ROV and inspection targets via acoustic pulses. This sensor is a suitable solution when the ROV operates in an environment with little bathymetry detail. For example, the ROV-Homer Target Relocation System is a miniature range and direction guidance system for ROVs, indicating the range to the targets and heading, depth information of ROV (Sonardyne, 2017). More positioning techniques can be found in (Capocci et al., 2017), such as dead

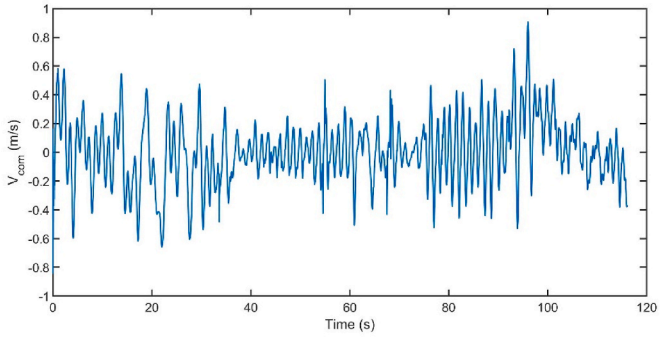

(a)

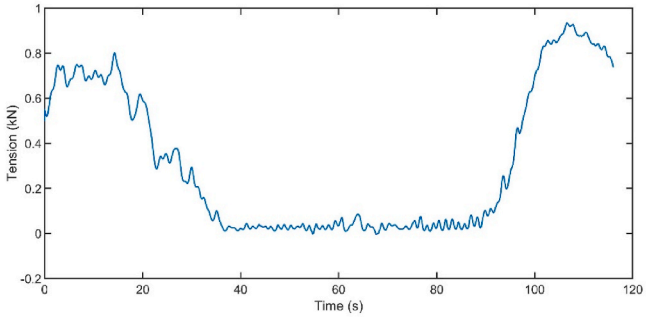

(b)

Fig. 17. Performance of the LARS in the scan surface case, (a)V_{COM} (b) umbilical tension.

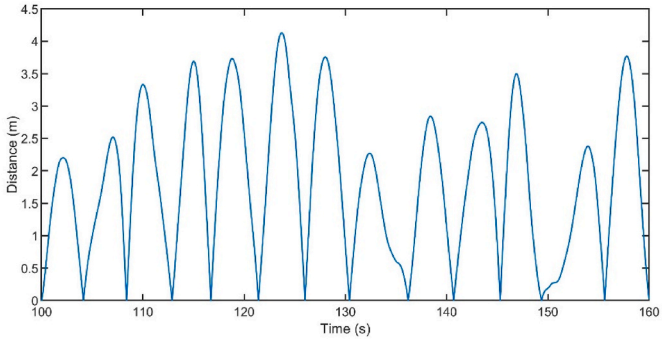

Fig. 18. Distance between ASV and ROV during the following stage.

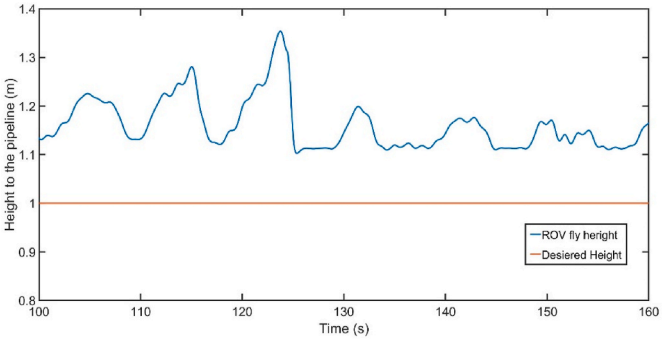

Fig. 19. ROV fly height during the pipeline check.

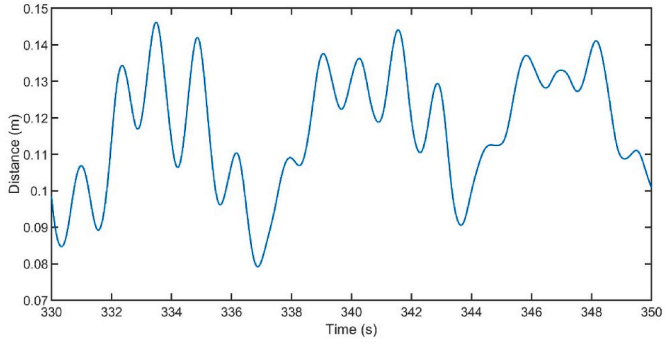

Fig. 20. Distance fluctuations between ROV and the target on z-direction in the last 20s.

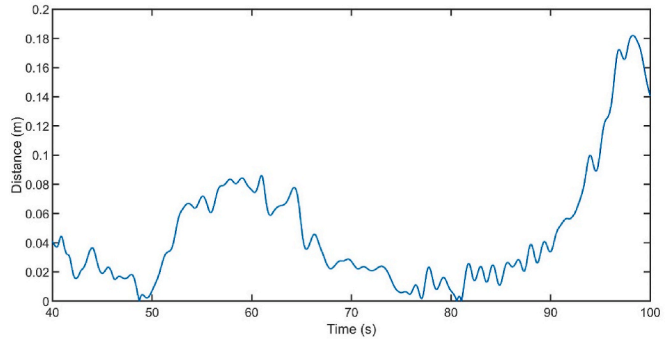

Fig. 21. Distance fluctuations between ROV and scan surface during the scan stage.

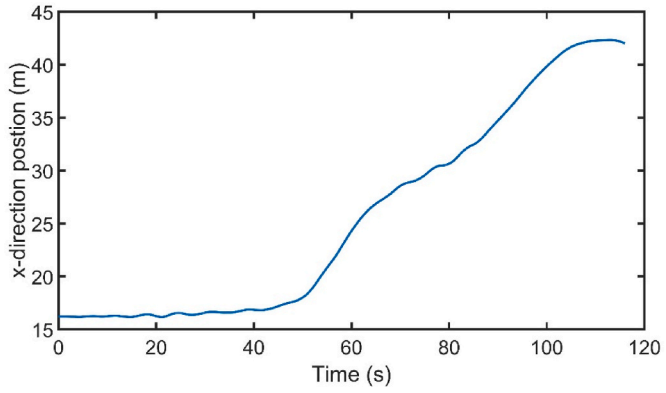

Fig. 22. Spar position in x-direction.

reckoning sensors, advanced ring laser and fibre optic gyros. With the development of the sensor technology, the ROV control strategy can be considered and designed with a more robust and higher frequency position feedback. The main scope of this study is to supply the method to modelling method of the ASV/ROV system and the inspection targets. Some parameters may not be suitable for the engineering application. As a result, the vital parameters of the ASV/ROV/winch control system should be carefully checked and designed based on the realistic requirements of the project.

This study's research methods have provided some new insights into the ASV/ROV application in offshore inspection. However, the applicability of the present model is explicitly discussed here. Firstly, as reported above, the constant winch speed has not been optimised in this study. The selected speed seems to be slightly too fast for the given ASV/

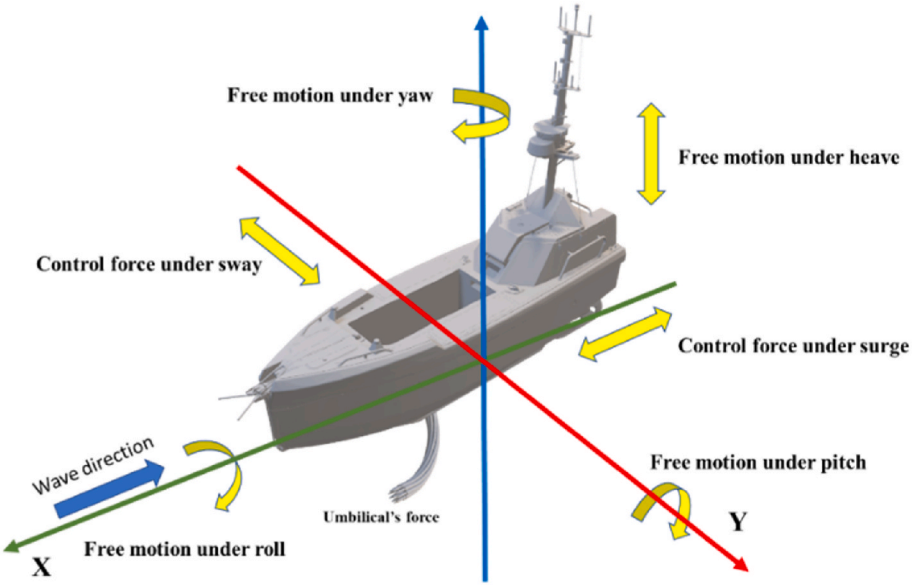

Fig. 23. The analytical model of the ASV: The control forces are applied in sway and surge directions.

ROV system in the FOWT cases, producing a potential collision risk between the umbilical and the spar. A variable speed will be used in further studies, based on the umbilical tension, bending radius, and length. Regarding the compensation winch, the target tension (1 kN) is too large for the given ASV/ROV system. It is found that the target tension (1 kN) will be automatically reduced via Eq. (10) because of the limitation of hydraulic cylinder/ram length. The method to quantify the most suitable target compensation target for LARS is subject to further work. Additionally, the ROV hydrodynamic coefficients will be changed by ASV and inspection targets, especially when the ROV is close to the ASV. This paper did not consider this change in the current stage. This would require a future experiment to quantify the exact coefficients for ROV proximity. Thirdly, more control strategies of the ASV/ROV can be designed and applied with the help of the presented model's high compatibility. Future work will aim to give a more robust and efficient control for both ASV and ROV. Finally, the additional hydrodynamic viscous damping of the ASV and ROV caused by the numerical approach (potential flow theory) should be refined through tank tests, where possible.

5. Conclusions

This paper modelled three generic offshore inspection missions suitable for ASV/ROV systems, namely pipeline inspection, mooring inspection and a circumferential FOWT surface scan. A fully coupled numerical model was built based on the frequency-time domain method, incorporating a range of control strategies and autonomous vessels. Key findings are summarised as follows:

- The distance between the ROV and inspection targets (includes both static and moving ones) fluctuates by the relative motion between ASV and ROV during check/scan stages, which require a fixed distance between ROV and targets. In this paper, the maximum fluctuation with the given ROV control is approximate 0.4 m in the pipeline check case and 0.15 m and 0.18 m in the FOWT mooring line check case and surface scan case, respectively.
- The net buoyancy of the ROV may produce a vertical offset, which should be considered in the control strategy. In this study, this offset is about 0.1 m.
- Compared to the 'static ASV', the 'following ASV' strategy can reduce the umbilical tension but will increase the distance fluctuations between the ROV and its inspection target.
- The hydrodynamic force caused by the tidal current can be used to help the ROV rotate/turn, when anticipated correctly.

This paper has provided the methodology and process to assess and design offshore inspection missions for autonomous ASV/ROV systems. The results show that these autonomous systems are highly capable of inspecting both static and moving targets.

CRediT authorship contribution statement

Chenyu Zhao: Writing – original draft, preparation. **Philipp R. Thies:** Visualization, Investigation. **Lars Johanning:** Supervision.

Declaration of competing interest

The authors declare that they have no known competing financial interests or personal relationships that could have appeared to influence the work reported in this paper.

Acknowledgements

This study has received funding through the project "Autonomous Robotic Intervention System For Extreme Maritime Environments (ARISE) Stage 2″, as part of the Industry Strategy Challenge Fund (ISFC) funded by Innovate U.K. (UKRI), Project Reference: 104831. The support through Orcina through the provision of their Orcaflex software also kindly acknowledged. The second author would also like to acknowledge funding through the EPSRC Supergen ORE Hub [EP/S000747/1].

Appendix

The analytical model of the ASV is illustrated in Fig. 23. Owing to the control forces and the umbilical force are nonlinear, the governing equations

(Yu et al., 2016) are presented under the time-domain as follows:

$$[M+m_\infty]\ddot{\xi}(t)+\int_{-\infty}^{t}H(t-\tau)\dot{\xi}(\tau)d\tau+([K]+[C])\xi(t)+[F_u(t)]=[F_e(t)] \tag{19}$$

where $[M+m_\infty]$ is the mass matrix under 6-DOFs (including the added mass matrix for $\omega\to\infty m_\infty$), $H(t)$ is the retardation function matrix which can be obtained from the convolution integrals of frequency-dependent damping matrix H_d presented by (Cummins, 1962; Greco et al., 2009), $[K]$ is the hydrostatic stiffness matrix, $[C]$ is the control force matrix, ξ is the ASV's motion equation, $[F_u]$ is the umbilical's force matrix and $[F_e]$ is the wave excitation force matrix.

The umbilical and winch system couples the ASV and the ROV. Thus, the crucial task is to determine the umbilical dynamics. According to (Ablow and Schechter, 1983), umbilical dynamics can be generally expressed as:

$$\mathbf{A}\frac{\partial \mathbf{y}}{\partial s}=\mathbf{B}\frac{\partial \mathbf{y}}{\partial t}+\mathbf{q} \tag{20}$$

with

$$\mathbf{A}=\begin{bmatrix}1&0&0&0&0&0\\0&1&0&0&V_b\cos\beta&-V_n\\0&0&1&0&-V_b\sin\beta&V_t\\0&0&0&1&V_n\sin\beta-V_t\cos\beta&0\\0&0&0&0&-T_{tension}\cos\beta&0\\0&0&0&0&0&T_{tension}\end{bmatrix}$$

$$\mathbf{B}=\begin{bmatrix}-m_u e\dfrac{V_t}{1+eT_{tension}}&m_u&0&0&(m_{u1}V_b-\rho S_u J_b)\cos\beta&-(m_{u1}V_n-\rho S_u J_n)\\e&0&0&0&0&0\\0&0&0&0&0&1+eT_{tension}\\0&0&0&0&(1+eT_{tension})\cos\beta&0\\-e\dfrac{m_{u1}V_b-\rho S_u J_b}{1+eT_{tension}}&0&0&m_{u1}&(m_{u1}V_n-\rho S_u J_n)\sin\beta-m_u V_t\cos\beta&0\\-e\dfrac{m_{u1}V_n-\rho S_u J_n}{1+eT_{tension}}&0&m_{u1}&0&-(m_{u1}V_b-\rho S_u J_b)\sin\beta&m_u V_t\end{bmatrix}$$

$$\mathbf{q}=\begin{bmatrix}w_u\sin\beta+\dfrac{1}{2}\rho d\sqrt{1+eT_{tension}}\pi C_t U_t|U_t|\\0\\0\\0\\\dfrac{1}{2}\rho d\sqrt{1+eT_{tension}}C_n U_b\sqrt{U_b^2+U_n^2}-\rho S_u\dot{J}_b\\w_u\cos\beta+\dfrac{1}{2}\rho d\sqrt{1+eT_{tension}}C_n U_n\sqrt{U_b^2+U_n^2}-\rho S_u\dot{J}_n\end{bmatrix}$$

where $\mathbf{y}$ is the dynamic vector of the umbilical, $\mathbf{y}(s,t)=[\ T_{tension}\quad V_t\quad V_n\quad V_d\quad \alpha\quad \beta\ ]^T$; s is the arc length of the cable between the ASV and ROV; t is the time; $\mathbf{V_u}=[\ V_t\quad V_n\quad V_d\ ]^T$ is the umbilical velocity matrix in its local coordinate; $T_{tension}=K_u\Delta l$, K_u is the spring coefficient, Δl is the deformation of the umbilical; m_u is the mass per unit length of umbilical; S_u is the cross-sectional area of the unstretched umbilical; e is the $1/ES_u$, E is the Young's modulus; m_{u1} denotes $m_u+\rho S_u$; The tidal current speed matrix in the umbilical coordinate is $\mathbf{J_u}=[J_t\quad J_n\quad J_d\ ]^T$, and the relative speed between umbilical and current can be written as $\mathbf{V_u}-\mathbf{J_u}=[U_t\quad U_n\quad U_d\ ]^T$; w_u is the $(m_u-\rho S_u)g$, g is the gravity acceleration.

To obtain the solution of equation (20), six boundary conditions will be needed. The two ends of the umbilical share the pay-out/in speed and the ROV speed, respectively. Thus, three boundary conditions are obtained.

For the ROV connection point, the ROV speed/angular speed on the $[\mathbf{t}\quad \mathbf{n}\quad \mathbf{b}\ ]$ can be denoted as

$$\mathbf{V_{ROV-tnb}}=[\ V_{ROV-t}\quad V_{ROV-n}\quad V_{ROV-b}\ ]^T \tag{21}$$

$$\Omega_{\mathbf{ROV}}=[\ u_{ROV-pitch}\quad v_{ROV-roll}\quad w_{ROV-yaw}\ ]^T \tag{22}$$

The relationship between ROV and umbilical coordinate could be expressed as:

$$[\mathbf{t}\quad \mathbf{n}\quad \mathbf{b}\ ]=[\ \mathbf{x_{ROV}}\quad \mathbf{y_{ROV}}\quad \mathbf{z_{ROV}}\ ]R_{ROV}^T(\theta_{ROV}\quad \varphi_{ROV}\quad \gamma_{ROV})W(\alpha,\beta) \tag{23}$$

In terms of (21) - (23), the boundary conditions (three boundaries) of ROV connected point could be obtained.

$$\mathbf{V_{ROV-connect}}(0,t)=(\mathbf{V_{ROV-tnb}}+\mathbf{\Omega_{ROV}}\times\mathbf{r_{ROV}})R_{ROV}(\theta_{ROV}\quad \varphi_{ROV}\quad \gamma_{ROV})W(\alpha,\beta) \tag{24}$$

Here, the length of umbilical at this point is considered as 0, $\mathbf{r_{ROV}}$ is the distance between the mass centre and the connecting point on the ROV. At the winch connected point, the umbilical speed at $\mathbf{b}$, $\mathbf{n}$ direction is zero:

$$\mathbf{V}_{\mathbf{n-winch-connect}}(s,t)=0 \tag{25}$$

$$\mathbf{V}_{\mathbf{b-winch-connect}}(s,t)=0 \tag{26}$$

The last boundary condition is obtained through the dynamic equation of the winch based on Newton's Law:

$$J_{winch}\dot{\mathbf{V}}_{\mathbf{t-winch-connect}}(s,t)=(F_{drive}-T_{tension}-F_{resistance})R_{winch} \tag{27}$$

where J_{winch} is the moment of inertia of the drum, $F_{resistance}$ is the resistance of the drum, R_{winch} is the radius of the drum.

The six boundary conditions [(16) to (20)] can be used to solve the equation (13). In the real sea environment, the $\mathbf{V}_{\mathbf{t-winch-connect}}(s,t)$ is always non-zero and dependent on the winch control method. The boundaries and solutions with a non-zero $\mathbf{V}_{\mathbf{t-winch-connect}}(s,t)$ are described in (Feng and Allen, 2004).

References

Ablow, C., Schechter, S., 1983. Numerical simulation of undersea cable dynamics. Ocean. Eng. 10 (6), 443–457.

Administration, U., 2021. Pipeline incident 20 Year trends. D. o. T. P. a. H. M. S. http://phmsa.dot.gov/pipeline/library/data-stats.

Ansys, A., 2013. In: Canonsburg, P.A. (Ed.), AQWA Theory Manual, vol. 15317 (USA).

Books, H., 1996. A Guide to the Pipelines Safety Regulations 1996.

Braathen, N., Sandford, A., 1986. Pipeline inspection by ROV. In: Submersible Technology. Springer, pp. 313–318.

Capocci, R., Dooly, G., Omerdić, E., Coleman, J., Newe, T., Toal, D., 2017. Inspection-class remotely operated vehicles—a review. J. Mar. Sci. Eng. 5 (1), 13.

Carroll, J., McDonald, A., McMillan, D., 2016. Failure rate, repair time and unscheduled O&M cost analysis of offshore wind turbines. Wind Energy 19 (6), 1107–1119.

Choi, J., Lee, Y., Kim, T., Jung, J., Choi, H.-T., 2017. Development of a ROV for Visual Inspection of Harbor Structures. IEEE Underwater Technology (UT), 2017.

Christ, R.D., Wernli Sr, R.L., 2011. The ROV Manual: a User Guide for Observation Class Remotely Operated Vehicles. Elsevier.

Conte, G., De Capua, G., Scaradozzi, D., 2016a. Designing the NGC system of a small ASV for tracking underwater targets. Robot. Autonom. Syst. 76, 46–57.

Conte, G., Scaradozzi, D., Animobono, D., 2020. A 4G robotic platform for shallow water operations. In: The 30th International Ocean and Polar Engineering Conference.

Conte, G., Scaradozzi, D., Mannocchi, D., Raspa, P., Panebianco, L., Screpanti, L., 2016b. Experimental testing of a cooperative ASV-ROV multi-agent system. IFAC-PapersOnLine 49 (23), 347–354.

Cummins, W., 1962. The Impulse Response Function and Ship Motions.

Fazeres-Ferradosa, T., Rosa-Santos, P., Taveira-Pinto, F., Vanem, E., Carvalho, H., Correia, J., 2019. Advanced research on offshore structures and foundation design: part 1. In: Proceedings of the Institution of Civil Engineers-Maritime Engineering.

Feng, Z., Allen, R., 2004. Evaluation of the effects of the communication cable on the dynamics of an underwater flight vehicle. Ocean. Eng. 31 (8–9), 1019–1035.

Gordon, R.B., Brown, M.G., Allen, E.M., 2014. Mooring Integrity Management: a State-Of-The-Art Review. Offshore Technology Conference.

Greco, M., Colicchio, G., Faltinsen, O., 2009. Bottom slamming for a very large floating structure: uncoupled global and slamming analyses. J. Fluid Struct. 25 (2), 406–419.

Hansen, R.E., Sæbø, T.O., Callow, H.J., Hagen, P.E., 2010. Interferometric Synthetic Aperture Sonar in Pipeline Inspection, vol. 10. IEEE SYDNEY. OCEANS.

Ho, M., El-Borgi, S., Patil, D., Song, G., 2020. Inspection and monitoring systems subsea pipelines: a review paper. Struct. Health Monit. 19 (2), 606–645.

Huster, A., Bergstrom, H., Gosior, J., White, D., 2009. Design and Operational Performance of a Standalone Passive Heave Compensation System for a Work Class ROV. OCEANS, 2009.

Jonkman, J., Butterfield, S., Musial, W., Scott, G., 2009. Definition of a 5-MW Reference Wind Turbine for Offshore System Development.

Jung, D.W., Hong, S.M., heon Lee, J., Cho, H.J., Choi, H.S., 2018. A study on unmanned surface vehicle combined with remotely operated vehicle system. Proceedings of Engineering and Technology Innovation 9, 17.

Khojasteh, D., Khojasteh, D., Kamali, R., Beyene, A., Iglesias, G.J.R., Reviews, S.E., 2018. Assessment of Renewable Energy Resources in Iran; with a Focus on Wave and Tidal Energy, vol. 81, pp. 2992–3005.

L3HARRIS, 2020. C-Worker 7. https://www.asvglobal.com/product/c-worker-7/. Retrieved 19/02 from.

Mandache, C., Clapham, L., 2003. A model for magnetic flux leakage signal predictions. J. Phys. Appl. Phys. 36 (20), 2427.

Manual, O. (2012). Online at http://www. orcina. com/SoftwareProducts/OrcaFlex/ Documentation. OrcaFlex. pdf.

Marció, B.S., Nienheysen, P., Habor, D., Flesch, R.C., 2019. Quality assessment and deviation analysis of three-dimensional geometrical characterization of a metal pipeline by pulse-echo ultrasonic and laser scanning techniques. Measurement 145, 30–37.

Marques, F.C., Demma, A., 2008. Ultrasonic guided waves evaluation of trials for pipeline inspection. In: Proceedings of the 17th World Conference on Non Destructive Testing. Shanghai, China.

Martinez-Luengo, M., Shafiee, M., 2019. Guidelines and cost-benefit analysis of the structural health monitoring implementation in offshore wind turbine support structures. Energies 12 (6), 1176.

Menegaldo, L.L., Ferreira, G.A.N., Santos, M.F., Guerato, R.S., 2009. Development and navigation of a mobile robot for floating production storage and offloading ship hull inspection. IEEE Trans. Ind. Electron. 56 (9), 3717–3722.

Menegaldo, L.L., Santos, M., Ferreira, G.A.N., Siqueira, R.G., Moscato, L., 2008. SIRUS: a mobile robot for floating production storage and offloading (FPSO) ship hull inspection. In: 2008 10th IEEE International Workshop on Advanced Motion Control.

Negahdaripour, S., Firoozfam, P., 2006. An ROV stereovision system for ship-hull inspection. IEEE J. Ocean. Eng. 31 (3), 551–564.

OrcaFlex, 2021. https://www.orcina.com/resources/examples/?key=k.

Organisation, G.O.W.H.S., 2020. 2019 incident data report. https://www.gplusoffshorewind.com/work-programme/statistics.

Rose, J.L., 2004. Ultrasonic Guided Waves in Structural Health Monitoring. Key Engineering Materials.

Salgado-Jimenez, T., Gonzalez-Lopez, J., Martinez-Soto, L., Olguin-Lopez, E., Resendiz-Gonzalez, P., Bandala-Sanchez, M., 2010. Deep Water ROV Design for the Mexican Oil Industry, vol. 10. OCEANS (IEEE SYDNEY).

Sarda, E.I., Dhanak, M.R., 2016. A USV-Based automated launch and recovery system for AUVs. IEEE J. Ocean. Eng. 42 (1), 37–55.

Seaeye, S., 2020. Falcon. https://www.saabseaeye.com/index.php/solutions/underwater-vehicles/falcon.

Sheppard, R.E., Puskar, F., Waldhart, C., 2010. SS: offshore wind energy special session: inspection guidance for offshore wind turbine facilities. In: Offshore Technology Conference.

Shi, Y., Zhang, C., Li, R., Cai, M., Jia, G., 2015. Theory and application of magnetic flux leakage pipeline detection. Sensors 15 (12), 31036–31055.

Sivčev, S., Omerdić, E., Dooly, G., Coleman, J., Toal, D., 2017. Towards inspection of marine energy devices using rovs: floating wind turbine motion replication. In: Iberian Robotics Conference.

Skjelvareid, M.H., Birkelund, Y., Larsen, Y., 2013. Internal pipeline inspection using virtual source synthetic aperture ultrasound imaging. NDT E Int. 54, 151–158.

Sonardyne, 2017. ROV-homer target relocation system. https://www.sonardyne.com/app/uploads/2016/06/ROV-Homer.pdf.

Tanimola, F., Hill, D., 2009. Distributed fibre optic sensors for pipeline protection. J. Nat. Gas Sci. Eng. 1 (4–5), 134–143.

Trslić, P., Rossi, M., Sivčev, S., Dooly, G., Coleman, J., Omerdić, E., Toal, D., 2018. Long Term, Inspection Class ROV Deployment Approach for Remote Monitoring and Inspection. OCEANS 2018 MTS/IEEE Charleston.

Wang, Q., Wang, X., 2010. Interferometeric fibre optic signal processing based on wavelet transform for subsea gas pipeline leakage inspection. In: 2010 International Conference on Measuring Technology and Mechatronics Automation.

Wang, W., Chen, X., Marburg, A., Chase, J., Hann, C., 2008. A low-cost unmanned underwater vehicle prototype for shallow water tasks. In: 2008 IEEE/ASME International Conference on Mechtronic and Embedded Systems and Applications.

Yu, Z., Shen, Y., Amdahl, J., Greco, M., 2016. Implementation of linear potential-flow theory in the 6DOF coupled simulation of ship collision and grounding accidents. J. Ship Res. 60 (3), 119–144.

Yuh, J., 1990. Modeling and control of underwater robotic vehicles. IEEE Transactions on Systems, man, and Cybernetics 20 (6), 1475–1483.

Yuh, J., Marani, G., Blidberg, D.R., 2011. Applications of marine robotic vehicles. Intelligent service robotics 4 (4), 221.

Zhao, C., Thies, P., Johanning, L., Tobin, S., 2020. Modelling and Assessment of ROV Capacity within an Autonomous Offshore Intervention System.

Zhao, C., Thies, P., Lars, J., Cowles, J., 2021. ROV launch and recovery from an unmanned autonomous surface vessel–Hydrodynamic modelling and system integration. Ocean. Eng. 232, 109019.